

# SHAPES OF MOLECULAR CLOUD CORES AND THE FILAMENTARY MODE OF STAR FORMATION

CHARLES L. CURRY<sup>1</sup>

Department of Physics, University of Waterloo, Waterloo, ON N2L 3G1

and

Department of Physics and Astronomy, University of Western Ontario, London, ON N6A 3K7

Submitted to ApJ 03/15/02; accepted 05/15/02

## ABSTRACT

Using recent dust continuum data, we generate the intrinsic ellipticity distribution of dense, starless molecular cloud cores. Under the hypothesis that the cores are all either oblate or prolate randomly-oriented spheroids, we show that a satisfactory fit to observations can be obtained with a gaussian prolate distribution having a mean intrinsic axis ratio of 0.54. Further, we show that correlations exist between the apparent axis ratio and both the peak intensity and total flux density of emission from the cores, the sign of which again favours the prolate hypothesis. The latter result shows that the mass of a given core depends on its intrinsic ellipticity. Monte Carlo simulations are performed to find the best-fit power law of this dependence. Finally, we show how these results are consistent with an evolutionary scenario leading from filamentary parent clouds to increasingly massive, condensed, and roughly spherical embedded cores.

*Subject headings:* ISM: clouds — ISM: structure — Stars: formation

## 1. INTRODUCTION

Little is known with certainty about the intrinsic shapes of the dense molecular clouds that give birth to stars. The present situation is reminiscent of the analogous study of elliptical galaxies some thirty years ago, when relatively few tests had been performed on limited datasets. In that field, attempts to model the observed distributions of ellipticity, surface brightness, and velocity dispersion with axisymmetric objects (e.g., oblate or prolate spheroids) met with limited success (Merritt 1982). Additional kinematical data and  $N$ -body simulations have led to the conclusion that many ellipticals are, in fact, triaxial (Merrifield and Binney 1998).

While from a modelling perspective our understanding of molecular cloud shapes lags behind that of stellar systems, much can be learned by applying the same methods in this new arena. At the same time, it is important to keep in mind certain salient differences between the two contexts, aside from the obvious difference of scale. First and foremost, gaseous self-gravitating clouds are not collisionless systems. Agents such as thermal instability, pressure gradients, and magnetic fields, more or less unique to the ISM context, have all been shown to be important in various physical regimes. Second, studies of the most centrally condensed cores of molecular clouds reveal them to be not the isolated (or infinite) balls of dense gas considered by simple theory, but rather the lowest rung in a hierarchy of structure beginning with parsec-scale entities (giant molecular clouds). This aspect needs to be considered when theory is brought to bear upon intrinsic core properties.

Clues to core structure are beginning to be extracted from morphological studies. Early analyses were hampered by datasets of limited size, which reduced the statistical significance of the conclusions (David & Verschueren 1987; Myers et al. 1991; Ryden 1996). Nevertheless, under the hypothesis that each object is a spheroid randomly-oriented to the line of sight, each of these studies concluded that cores were more likely to be intrinsically prolate than oblate. The recent study of

Jones, Basu, & Dubinski (2001) analyzed the largest dataset to date: 264 ammonia cores compiled by Jijina, Myers, & Adams (1999). By showing that the best-fit probability distributions of prolate and oblate spheroids became negative near  $p = 1$ , these authors rejected the hypothesis of axisymmetry altogether. A closer examination of the analysis technique, however, gives a likely explanation of their results (see below §3).

All of the aforementioned analyses utilized but one observational diagnostic of core shape: the projected axis ratio, or ellipticity. However, as remarked by Fleck (1992), the *mean* value of this quantity cannot be used to distinguish one spheroidal shape over another. Moreover, as pointed out by Binney & de Vaucouleurs (1981) and Ryden (1996), the measurement of axis ratios is subject to various systematic biases that can affect the overall distribution and subsequent analysis. In fact, other physical properties—such as column density, velocity dispersion, and mass—have influenced theoretical models of cloud cores far more than have the perceived ellipticities. We feel that to abandon the hypothesis of axisymmetry in lieu of examining these diagnostics is premature, especially given the lack of a physical basis for triaxiality in the ISM context (akin to the anisotropic velocity distribution of stars in elliptical galaxies).

In §4 and 5, we employ a number of tests to discriminate between the oblate and prolate spheroidal hypotheses. Two of the tests are new in the ISM context, and the other—the distribution of projected axis ratios—has not previously been applied to the dust continuum data on which we base our analysis (however, subsets of these data were recently analyzed by Jones & Basu (2002), under the oblate and triaxial hypotheses only). Further, by simulating the observed sample using distributions of model cores of both types, we are able to place rather stringent constraints on one intrinsic property, the variation of polar intensity with intrinsic ellipticity. All of the tests are independent of distance, still a very uncertain quantity for these objects (see, e.g., Launhardt & Henning 1997).

Finally, in §6 we interpret our results in the framework of an evolutionary sequence of core shapes as a function of time.

<sup>1</sup>Email: curry@astro.uwaterloo.ca

In this picture, core morphology at early times is primarily determined by the nature of the surrounding nonisotropic mass distribution. As the core grows in mass, it approaches a spherical shape consistent with the dominance of self-gravity. As we shall see, this behavior is consistent with the present observational picture.

## 2. DATA

We analyzed recent dust continuum (submillimeter) observations of dense cores in three prominent star-forming regions: Orion OMC-2 and 3 (Chini et al. 1997),  $\rho$  Ophiuchus (Motte, André, & Neri 1998), and Orion B (Motte et al. 2001). Collectively, we refer to these observations, which identified a total of 165 dense cores, as the “combined continuum dataset.” The dust continuum data have at least two distinct advantages over molecular line measurements as a probe of core structure. First, while molecular lines have a limited range of both column and number density sensitivity (a factor  $\sim 10$ –30) due to opacity and molecular freeze-out onto grains, thermal emission from dust is presumably optically thin. This means that column (or continuum flux) densities are bounded only from below by detector sensitivity, while the derived number densities vary inversely with beam resolution (beam-averaged  $\text{H}_2$  column densities  $\gtrsim 10^{23} \text{ cm}^{-2}$  are typical; e.g., Testi & Sargent 1998). Second, while there is in most cases a rough spatial coincidence between the peaks seen in the dust continuum surveys and those seen in dense molecular tracers, the continuum cores may in fact be more representative of the progenitors of stars. This is suggested by the remarkable agreement between the mass spectrum of the cores and the field star initial mass function (Testi & Sargent 1998; Motte et al. 1998, 2001; Johnstone et al. 2000, 2001).

Since we make extensive use of the Motte et al. (2001) dataset (hereafter M01), we note here some of its properties used later in the analysis. The survey covered a  $32' \times 18'$  region of Orion B, including the NGC 2068/2071 protoclusters, and identified 82 dense condensations. We analyzed the  $850 \mu\text{m}$  data, for which the half-power beam width is  $R_B \simeq 13'' \approx 5000 \text{ AU}$  at the assumed distance of Orion B (400 pc). The one-sigma rms noise within the beam is  $\Delta I = 22 \text{ mJy/beam}$ . For a core with FWHM size  $R$ , the rms noise in the integrated (total) flux density  $S$  is  $\Delta S \approx 22 \text{ mJy} \times \sqrt{(R^2 + R_B^2)/R_B^2} \times 2 = 65 \text{ mJy}$  for  $R \simeq 5500 \text{ AU}$ , the mean core size in the sample. The absolute calibration uncertainty of the measurements is  $\sim 20\%$ . Only the total flux for each core was given in M01; peak intensities  $I$  (flux within a single beam) were obtained from the authors. The total error in  $\log I$  ranges between  $-0.22$  and  $+0.14$  over the range observed. We take the error in  $\log p$  to be  $\pm 0.05$ , as determined from the precision of M01’s figures for the core major and minor axes ( $\pm 200 \text{ AU}$ ).

While several dust continuum surveys of other regions are now available, we have used only those for which both apparent major/minor axes and peak intensities were tabulated. The reason for this will become clear presently.

## 3. THE DISTRIBUTION OF CORE ELLIPTICITIES

The frequency distribution of the apparent axis ratio  $p$  (apparent minor/major axis length  $\equiv b'/a'$ ) is the only tool used thus far in efforts to deduce the intrinsic shapes of molecular cloud cores. While prone to selection effects at both low and high ellipticity, the method can give some insight into the constraints involved (see §1 for references). The histogram in Fig-

ure 1a shows the distribution of core apparent axis ratios, using the combined continuum dataset. The mean value is  $\langle p \rangle = 0.63$  (median: 0.64), with a standard deviation of 0.20. This distribution is similar to that seen in the extensive and much more heterogeneous ammonia dataset of Jijina et al. (1999) (see Jones et al. 2001). In particular, both distributions are skewed towards  $p = 1$ : in Figure 1 there are more than twice as many objects with  $0.8 \leq p \leq 1$  than with  $0.1 \leq p \leq 0.3$ . This characteristic is particularly evident in the Chini et al. and Motte et al. (1998) samples, in which 86% and 79% of the cores, respectively, have  $p \geq 0.5$ .

Let the intrinsic frequency distribution of cores of intrinsic axis ratio  $q$  (intrinsic minor/major axis length  $\equiv b/a$ ) be denoted by  $\psi(q)$ . Then, if the cores are oriented randomly on the sky, the observed distribution  $\phi$  of apparent (projected) axis ratios  $p$  is given by (Noerdlinger 1979; Fall & Frenk 1983):

$$\phi(p) = p \int_0^p dq (1-q^2)^{-1/2} (p^2 - q^2)^{-1/2} \psi(q) \quad (\text{oblate}); \quad (1)$$

$$= p^{-2} \int_0^p dq q^2 (1-q^2)^{-1/2} (p^2 - q^2)^{-1/2} \psi(q) \quad (\text{prolate}). \quad (2)$$

The derivation of  $\psi(q)$  from the observed  $\phi(p)$  has been attempted in a number of ways. For example, Ryden (1996) employed a nonparametric kernel estimator, while Jones et al. (2001) used an analytic inversion method. Both replaced the observed distribution histogram with a smooth function before inverting to find  $\psi(q)$ . In the process, restrictions were placed on either the form of  $\phi(p)$  (an odd polynomial of degree 5; Jones et al.) or its slope at the endpoints ( $d\phi/dp = 0$ ; Ryden). Despite the fact that this biases any comparison of the observed and theoretical distributions, the goodness-of-fit criteria in both studies rely upon the behavior near the endpoints, particularly at  $p = 1$ . Thus, these authors’ finding that the probability distributions of spheroids become negative (for some samples) near  $p = 1$  needs to be re-established in the absence of such restrictions.

While a direct inversion method, such as the type devised by Lucy (1974) (and applied in the galactic context by Noerdlinger), would be the most robust means of deriving  $\psi(q)$ , our objective here is more modest. We seek merely to demonstrate that a reasonable distribution of randomly-oriented spheroids can reproduce the histogram of Figure 1a. We let  $\psi(q)$  equal a gaussian with mean value  $\langle q \rangle$  and dispersion  $\sigma$ , and generated  $\phi(p)$  from equations (1) and (2) for a range of values of these parameters.

The resulting  $\chi^2$  minimization fits to the observed histogram (now shown as a probability density) are shown in Figure 1b. While neither prolate nor oblate distributions give a completely satisfactory fit, the prolate distribution with  $\langle q \rangle = 0.54$  and  $\sigma = 0.19$  ( $\chi^2 = 0.28$ ) is clearly superior. The fit in the oblate case is less satisfactory:  $\langle q \rangle = 0.39$  and  $\sigma = 0.16$  with  $\chi^2 = 0.51$ . In this case, while the observed  $\phi$  can be fit at low  $p$ , the peak in the derived  $\phi$  lies at a smaller  $p$  than observed, and objects with nearly circular projections are over-produced. The best-fitting oblate distribution consists of cores that are intrinsically more flattened than in the prolate case, which also may be considered a priori less likely (Myers et al., 1991). While the poor agreement may simply be a result of restricting  $\psi$  to be gaussian, a less generic form of  $\psi$  used in the oblate, but not in the prolate, case has little justification.

We also applied the  $\chi^2$  analysis to the axis ratio distribution of Jijina et al. (1999). The same qualitative result was found, but with less of a difference between the oblate ( $\chi^2 = 0.97$ ) and prolate ( $\chi^2 = 0.88$ ) scenarios.<sup>2</sup> These results make clear that, despite recent claims to the contrary, the observed  $\phi(p)$  is reasonably well-fit by a gaussian distribution  $\psi(q)$  of randomly-oriented prolate spheroids. This consequently weakens the motivation for triaxial models which, in any case, have no theoretical basis in the context of gaseous, equilibrium clouds. We shall use these best-fit intrinsic distributions to generate peak intensities for simulated datasets in §5.

#### 4. OBSERVED CORRELATIONS

##### 4.1. Relation Between Peak Intensity and Apparent Ellipticity

Consider a cloud core in which the mass distribution is constant on similar ellipsoids, either oblate or prolate. In an optically thin tracer, the particular line of sight corresponding to the peak intensity  $I$  (or peak flux density; units Jy/beam) represents the complete column through the core.<sup>3</sup> It should therefore depend upon the apparent axis ratio  $p$ . Thus we have (Richstone 1979; Merritt 1982):

$$I(\theta) = \frac{q}{p} I_e = p^{-1} I_p \quad (\text{oblate}) \quad (3)$$

$$I(\theta) = \frac{p}{q} I_e = p I_p \quad (\text{prolate}), \quad (4)$$

where  $\theta$  is the angle between the observer's line of sight and the equatorial plane,  $I_e = I(0)$  is the intensity as seen toward the same plane, and  $I_p = I(\pi/2)$  is the intensity as seen down the polar axis. The intrinsic and apparent axis ratios,  $q$  and  $p$ , are related to  $\theta$  via

$$\cos^2 \theta = \frac{1-p^2}{1-q^2} \quad (\text{oblate}) \quad (5)$$

$$\sin^2 \theta = \frac{1-q^2/p^2}{1-q^2} \quad (\text{prolate}). \quad (6)$$

In both cases, the value  $p = 1$  refers to the case in which the object is viewed along the polar axis, and therefore has a circular projection.

Let us assume, in the first approximation, that: (i) the cores are randomly oriented, and (ii)  $I_p$  does not vary from one core to the next in a population of either all-oblate or all-prolate spheroids. Then the observed intensity  $I$  will increase towards  $p = 1$  in the prolate case, and decrease towards  $p = 1$  in the oblate case. Specifically, the expected slopes in a  $(\log I, \log p)$  plot are +1 and -1, respectively (throughout this paper,  $\log$  denotes  $\log_{10}$ ). [For applications in the context of elliptical galaxies, see Marchant & Olson (1979), Richstone (1979), and Olson & de Vaucouleurs (1981).]

In Figures 2 and 3 we plot the relation between  $\log I$  and  $\log p$  for each subsample of the combined continuum dataset. The sample of Chini et al. (1997) is shown in Figure 2a. This sample contains only 21 data points, and while there is some suggestion of an increasing trend of  $I$  with  $p$ , it is not statistically significant. The same is true of the Motte et al. (1998) data from Ophiuchus, shown in Figure 2b.

<sup>2</sup>The elevated  $\chi^2$  in both cases is due to a poor fit near  $p = 1$ , where the number of nearly circular objects more than doubles in the rightmost bin ( $0.9 \leq p \leq 1$ ). It is likely that the latter number has been overestimated in this more heterogeneous sample, due to rounding errors in older measurements (see, e.g., Ryden 1996).

<sup>3</sup>All intensities and flux densities referred to in this work are monochromatic, measured at either 850 or 1300  $\mu\text{m}$ .

<sup>4</sup>In doing so we err on the side of caution, since NGC 2071-IRS is still deeply embedded, with an extended envelope whose shape may still reflect the pre-stellar condition of the core.

While the above two samples show no significant trend, the Orion B dataset of M01 ( $N = 64$  resolved objects), shown in Figure 3a, is more definitive. Although there is considerable scatter, a correlation does exist between  $\log I$  and  $\log p$ . The linear (parametric) correlation coefficient (C.C.) is 0.35, with a significance of greater than 99 percent. Under the more general assumption that the underlying distributions of  $I$  and  $p$  are not binormal, we can perform the nonparametric Spearman and Kendall (rank correlation) tests. These give a coefficient of 0.29 and a significance of 98 percent. The point at  $(\log p, \log I) \simeq (-0.05, 4)$  is clearly an outlier. It corresponds to NGC 2071-IRS, a known outflow source. Since we wish to focus on starless cores in this study, we exclude it from further consideration.<sup>4</sup> This lowers the rank C.C. to 0.27 with a significance of 96.3 percent. The best-fit straight line to the data is given by  $\log I = A \log p + B$ , with  $A = 0.50 \pm 0.18$  and  $B = 2.56 \pm 0.06$ .

The above fit was performed neglecting the stated observational errors in  $\log I$  and  $\log p$  (§2). While this might be considered reprehensible, we found that including the errors gave a goodness-of-fit parameter that was too low to be acceptable by the usual standard ( $\gtrsim 10^{-3}$ ; Press et al. 1992). This result does not cast aspersions on the validity of the correlation stated above (which does not depend on the errors), nor need it necessarily lower our confidence in the fitted values of  $A$  and  $B$ . Rather, it is a familiar feature of data that have a scatter larger than the formal errors. In particular, it indicates that the uncertainties ascribed to  $I$  are *underestimates*. We present ample support for this statement, along with a consistency check of the above fitted parameters, in §5.5. There a more robust analysis is used to determine the model goodness-of-fit for the data (specifically, the Monte Carlo simulation of synthetic data sets).

Many of the cores (18/82, or 22 percent) in the sample are unresolved, and therefore are not included in the above fit. Interestingly, despite the fact that all are  $5\sigma$  detections, none has a peak intensity exceeding 0.25 Jy/beam. If the apparent ellipticities of the unresolved cores are distributed in the same way as the rest of the sample, this then suggests that there are more elongated than round sources amongst this sub-population.

Finally, we note that while the observed slope of the above fit is positive, it disagrees with the value of +1 expected if all of the cores are randomly-oriented, prolate spheroids with  $I_p = \text{const}$ . This feature will be addressed in §5.

##### 4.2. Relation Between Total Flux and Apparent Ellipticity

The observed intensity integrated over the core area, or total flux density,  $S$ , is a quantity of additional interest, since it is proportional to the core mass  $M$ . Again assuming the dust emission to be optically thin, the gas mass of a core is (Johnstone et al. 2000)

$$M = \frac{S d^2}{\kappa B(T_d)},$$

where  $d$  is the core distance,  $T_d$  the dust temperature,  $B$  the Planck function, and  $\kappa$  the dust opacity (the latter two evaluated at a specific frequency of interest). In the absence of any intrinsic dependence of  $S$  on  $q$ , it is clear that  $S$  *should be independent of  $p$ , since the emission is optically thin*. This furnishes

an important test of the hypothesis that the observations can be reproduced by a population of more or less identical (i.e.,  $I_p \approx$  constant), randomly-oriented cores.

A log-log plot of  $S$  vs.  $p$  for the M01 sample is shown in Figure 3b. It shows that  $S$  exhibits a strong positive correlation with  $p$ . Again omitting NGC 2071-IRS, the linear correlation coefficient is 0.37, with a significance of greater than 99 percent. The rank correlation is 0.31 with a significance of 98.7 percent. The best-fit straight line to the data has  $A = 0.65 \pm 0.21$  and  $B = 2.84 \pm 0.06$ . Thus it appears that *intrinsic effects do play a role in producing the observed peak intensity and mass distribution of the cores*. The dependence of  $I$  and  $M$  on  $q$  implied by this result will be examined in §5.

Another interesting property of the total flux is the degree to which it tracks the peak intensity  $I$ . A log-log plot of  $S$  versus  $I$  yields a tight correlation with a rank C.C. of 0.89 (probability of no correlation  $< 10^{-4}$ ) and a slope of  $1.17 \pm 0.06$ . This is not that surprising given that the mean core size  $\langle R \rangle \simeq 5500$  AU just exceeds the beam size of 5000 AU. However, it is easier to reconcile with an intrinsically prolate distribution in the following respect. Members of the latter population, having  $b' = b$ , will more often be viewed near the resolution limit, since  $\langle b' \rangle = 4600 \pm 2900$  AU. In the oblate case, however,  $\langle a' \rangle = 7800 \pm 4500$  AU, so that nearly all objects are greater than the beam size in extent, leading to a bigger expected difference between  $S$  and  $I$ .

Finally, by plotting  $\log S$  versus the  $\log$  of the core size  $R \equiv (a'b')^{1/2}$ , we find—confirming the conclusion of M01—that  $S \propto R^{1.1}$ . This is close to the  $M \propto R$  relation expected for a gaseous sphere in virial equilibrium, suggesting that the cores are self-gravitating.

## 5. INTRINSIC CORRELATIONS

### 5.1. General Considerations

The results of the previous section imply that  $I$  depends upon intrinsic properties of the core. We first ask whether there exist any systematic trends that could contribute to the correlations seen in Figure 3. For instance, were the size of the cores to increase with increasing  $q$ —irrespective of any assumption about intrinsic shape—then both  $I$  and  $S$  would be seen to increase with  $p$ .

To look for such an effect, we plotted  $\log I$  vs.  $\log R$  and the observed FWHM major axis  $\log a'$  vs.  $\log p$  in Figures 4a and b, respectively. In the first plot, no correlation is seen—although the highest flux point, NGC2071-IRS, has one of the largest inferred sizes. A curious feature of the second plot is the exactly linear slope of  $-1$  seen in the subset of points at lower left. This is a resolution effect: all nine objects have a projected minor axis  $b' = 1600$  AU, the smallest in the sample. Since  $p = b'/a'$ , each point lies on a single line of slope  $-1$  in the  $\log a' - \log p$  plane. Several such alignments can be seen in the plot, reflecting the finite spatial resolution of 200 AU. Statistically, however, there is no significant correlation between the two quantities. Finally, the observed size distribution of the cores is close to gaussian, with  $\langle \log R \rangle = 3.74 \pm 0.17$ .

In the absence of a systematic variation in scale with  $p$ , there remains the possibility of an intrinsic dependence of  $I_p$  on  $q$

[equations (3) and (4)]. In the context of elliptical galaxies, Merritt (1982) showed that such a dependence can completely mask or even reverse the expected correlation in  $(\log I, \log p)$ . Following his analysis, we begin by assuming that  $I_p$  depends only on  $q$ , and write

$$I_p = q^m I_0, \quad (7)$$

where  $I_0 = \text{constant}$  and  $m \neq 0$  (the discussion of the previous section assumed  $m = 0$ ). As Merritt demonstrated, a positive slope of unity in  $(\log I, \log p)$  may be obtained either by assuming that all objects are prolate with  $m$  near zero, or that all objects are oblate with  $m$  large and positive. Further, once observational errors were added, simulated data corresponding to, say, a prolate population with  $m = 0$  and an oblate population with  $m = 3$  became formally indistinguishable.<sup>5</sup> It is desirable to determine what range of  $m$  values may be expected in the context of molecular clouds. Here we turn to theoretical considerations which, however crude, can be used to obtain rough constraints on this parameter.

### 5.2. Oblate clouds

Several studies of isolated oblate clouds—the prevailing theoretical paradigm for the precursors of protostars—have established the relation between ellipticity and mass: in general, both increase together. This is true irrespective of whether the flattening is caused by rotation (Stahler 1983; Kiguchi et al. 1987) or flow down polar magnetic field lines (Tomisaka, Ikeuchi, & Nakamura 1988; Nakamura, Hanawa, & Nakano 1995), provided that only those equilibrium sequences along which the equatorial radius is roughly constant are considered.<sup>6</sup> It is the tendency of gravity to enhance elongation along the shorter axis (i.e.,  $q \propto M^{-\alpha}$ ,  $\alpha > 0$ ) that is responsible for the flattening in both cases.

In order to relate  $M$  to the assumed form of  $I_p$ , first recall that  $S \simeq I^{1.17}$  in the M01 sample. In general, we expect  $S \sim I^{1+C}$ , where  $C > 0$  is a constant. Then, since  $M \propto S$ , we have

$$M \sim I^{1+C} = (p^{-1} I_p)^{1+C} = (p^{-1} q^m I_0)^{1+C}. \quad (8)$$

According to equation (5),  $p$  ranges from  $q$  to unity depending upon orientation, so  $M \sim q^{(m-1)(1+C)}$  if all cores are observed edge-on and  $M \sim q^{m(1+C)}$  if all are pole-on. In order for  $M$  to increase with decreasing  $q$  then, *we must at the very least have  $m < 1$  in the oblate case*. This result agrees qualitatively with that obtained in the special case of a uniform, isothermal (sound speed =  $c_s$ ), self-gravitating disk (Fleck 1992):

$$M \simeq \frac{c_s^2 a}{2G} q^{-1},$$

which corresponds to  $\alpha = 1$  in the above canonical form (recall that  $a$  is the major axis length). Larger or smaller values of  $\alpha$  might apply to less flattened configurations, a non-isothermal equation of state, and/or an inhomogeneous matter distribution. In any event, it would appear that *in the oblate case, the large positive values of  $m$  required to produce a positive slope in  $(\log I, \log p)$  are effectively ruled out*.

<sup>5</sup>Note that Merritt adopted a different convention for  $p$  from that used here ( $p < 1$  in the oblate case;  $p > 1$  for prolate), used a different intrinsic distribution  $\psi(q)$ , and plotted  $|\log p|$  on the horizontal axis. Hence, the signs and values of his slopes generally differ from ours.

<sup>6</sup>In the magnetic case, such a sequence has a constant ratio of magnetic pressure at infinity to cloud surface pressure. In the rotating models, the ratio of the rotational to gravitational energy at the cloud surface is held fixed. Both of these assumptions are reasonable if members of the sequence are taken to represent different stages of condensation—within a single parent cloud—in the approach to dynamical collapse.

### 5.3. Prolate clouds

The lack of a theoretical paradigm for prolate clouds precludes a similarly firm prediction in this case. However, from the few studies that exist (Hanawa et al. 1993; Curry 2000; Fiege & Pudritz 2000a; Balsara et al. 2001), certain key properties may be anticipated. First, prolate clouds are not likely to be isolated, but rather should be embedded in larger, filamentary structures.<sup>7</sup> Second, the behavior of an embedded core's mass and density as a function of its intrinsic axis ratio is such that the latter rises to near unity at high mass and central concentration (Curry 2000; Fiege & Pudritz 2000b). Thus, a prolate core condensing out of its parent filament should approach an approximately spherical shape at large mass, or equivalently, at a late evolutionary stage as a pre-stellar object.

The analogous expression to equation (8) in the prolate case is

$$M \sim I^{1+C} = (p I_p)^{1+C} = (p q^m I_0)^{1+C}. \quad (9)$$

With  $p$  again ranging between  $q$  and unity, this gives  $M \sim q^{(m+1)(1+C)}$  if all the cores are edge-on and  $M \sim q^{m(1+C)}$  if all are pole-on. In order for  $M$  to increase with increasing  $q$  then, we must at the very least have  $m > -1$  in the prolate case.

### 5.4. Consequences for the observed correlations

These predictions for the expected range of  $m$  in the two cases should be taken as rough guidelines; exceptions can surely be found. However, to the extent that they are reasonably robust, they lead to the following conclusions. Using equations (3), (4), and (7), we write the  $\log I$ – $\log p$  relation as

$$\log I = \pm \log p + m \log q + \log I_0,$$

where the upper (lower) sign on the right-hand side applies to the prolate (oblate) case. In the oblate case, it is clear that the effect of an intrinsic dependence of  $I_p$  on  $q$  with  $m < 0$  is an *increase* in the mean slope of the  $\log I$ – $\log p$  relation from its  $m = 0$  value of  $-1$ . A decrease in slope can only occur if  $0 < m < 1$ ; however, the slope is still limited to negative values, since  $q \leq p$ . In the prolate case, on the other hand, the expected dependence of  $I_p$  on  $q$  leads to a *decrease* in the slope if  $-1 < m < 0$ , and an *increase* if  $m > 0$ . This suggests that small negative values of  $m$  may be consistent with the observed slope of the  $(\log I, \log p)$  relation. We test this hypothesis in the following subsection.

### 5.5. Simulations

Using the relations found in this and the previous sections, Monte Carlo simulations were carried out for a sample of 65 model cores. Each simulation consisted of 1000 realizations of a given model. In detail, the procedure was as follows. (1) Each core was randomly assigned an intrinsic ellipticity from the best-fit gaussian distribution (either oblate or prolate) derived in §3. (2) The angle of observation was randomly chosen from a uniform distribution over the sphere. (3) The intrinsic flux  $\log I_0$  was, in the first instance, set equal to 2.45, the mean of the observed dataset. (4) Normal distributions of measurement error were added randomly to both  $p$  and  $I$ . In accord with the uncertainties cited in M01 and §2, we assigned dispersions of 0.05 in  $\log p$  and 0.15 in  $\log I$ . (5) In order to test the hypothesis that some of the scatter in the observational plot might be intrinsic to the cores, we also ran simulations in which an ad hoc

variation of  $\pm 0.15$  in  $\log I_0$  was added to some of the realizations. This intrinsic scatter could, e.g., reflect a dependence on an unknown parameter, or simply be due to random differences in formation or past history of individual objects. (6) Finally, using equations (8) and (9), we calculated  $S$  for each simulated core.

The results are given in Tables 1 ( $\log I$  vs.  $\log p$ ) and 2 ( $\log S$  vs.  $\log p$ ). Calculations were performed for values of  $m$  appropriate to the ranges derived in the previous subsections. For each model there are two entries: the mean slope and the rank correlation coefficient, averaged over all 1000 realizations of the model, and their dispersions. A model was judged a good fit to the observations at the  $1\sigma$  level if the observed values of both the slope and correlation coefficient (Figure 3a) fell within the  $1\sigma$  confidence intervals of the Monte Carlo simulations.

As expected from the results of the preceding subsection, the oblate model slopes in the  $(\log I, \log p)$  plane are negative in the range examined, while prolate models have positive slopes (see Table 1). Evidently, introducing an intrinsic scatter in  $I_0$  hardly alters the derived slopes; only the dispersions are affected. Not surprisingly, the correlation coefficients are also lowered in models with intrinsic scatter, particularly near  $m = 0$  (oblate) and  $m = -1$  (prolate). Note that the simulations correctly reproduce (within the dispersions) the expected slopes for  $m = 0$ ; namely  $-1$  and  $+1$  in the oblate and prolate cases, respectively.

Comparing now with the observed correlation in  $\log I$ – $\log p$  (slope =  $0.50 \pm 0.18$ , rank C.C. = 0.27; Figure 3a), we see that a prolate model with  $-1 < m < -0.5$  is likely to reproduce the observed parameters. Specifically, it is found that for  $m = -0.60$  and  $\sigma(\log I_0) = 0.15$ , the simulated slope and C.C. are  $0.50 \pm 0.15$  and  $0.26 \pm 0.08$ , respectively. Therefore, this set of prolate models is in agreement with the observations at the  $1\sigma$  level. One realization from this suite of simulations is shown in Figure 5a.

The  $S$  vs.  $p$  results given in Table 2 provide an important, although not entirely independent, consistency check of these results. The above best-fit simulation with  $\sigma(\log I_0) = 0.15$  and  $m = -0.60$  has a slope (in the  $\log S$ – $\log p$  plane) of  $0.59 \pm 0.16$  and a rank C.C. of  $0.28 \pm 0.08$ , respectively. While a better fit to the data of Figure 3b could be found for a slightly larger value of  $m$ , we do not feel that this would be as reliable a determination as that found above, given the uncertainties in the  $S(q)$  relations derived in §5.1. A realization from this suite of simulations is shown in Figure 5b.

Recall that, in §4.1, the linear least-squares fit *with errors* to the observed  $(\log I, \log p)$  gave a goodness-of-fit parameter that was too low to be acceptable. It is worth checking whether the addition of the intrinsic scatter in  $I_0$  rectifies this situation. Upon doing so, we found a slope of  $0.59 \pm 0.20$  and intercept of  $2.60 \pm 0.06$ , with a goodness-of-fit equal to 0.41. These values are in agreement with those found ignoring the errors in §4.1, thus providing an extra measure of confidence in the fitting parameters derived there.

Finally, it is interesting to ask whether a satisfactory fit of the oblate models to observations could be obtained if  $m$  were unrestricted. Surprisingly, the answer is no: while a slope of  $0.50 \pm 0.88$  in  $(\log I, \log p)$  is obtained for  $m = 4.2$  in the oblate case, the corresponding rank C.C. equals  $0.02 \pm 0.08$ , indicating no correlation. This means that the underlying distribution

<sup>7</sup>While isolated prolate equilibria have been constructed using specific magnetic field geometries (Fiege & Pudritz 2000b; Curry & Stahler 2001), these can hardly be considered generic.

of axis ratios  $\psi(q)$  prohibits such a correlation. Thus, we conclude that the oblate hypothesis can be rejected with the same degree of confidence.

## 6. DISCUSSION

### 6.1. Intrinsic Correlations: Theory

Here we compare the results obtained above with a particular class of prolate equilibria: the embedded, isothermal cores of Curry (2000). The equilibrium sequence is characterized by a single parameter,  $2Z$ : the length of the parent cylindrical cloud, as compared with the critical wavelength for instability along its major axis,  $\lambda_{\text{cr}}$ . The embedded condensations exist only for  $2Z > \lambda_{\text{cr}}$ . In standard cylindrical coordinates, the point  $r = 0$ ,  $z = Z$  represents a saddle point between two adjacent cores. The cores themselves are defined by the tidal lobe, the constant-density surface extending from  $(0, Z)$  to  $(0, -Z)$  through the point  $(R_{\text{tl}}, 0)$  in the midplane (see Figure 2 of Curry 2000). It is desirable to calculate the variation of both the polar intensity (or column density) and the mass of the embedded cores as a function of intrinsic ellipticity in these models.

We are immediately confronted with the issue of how to define the above quantities in the context of an embedded core. Specifically, what are the appropriate theoretical definitions of  $I_p$  and  $M$ ? The former is proportional to the column density along the core major axis,

$$N_p = \int_{-Z}^Z \rho(0, z) dz. \quad (10)$$

As  $Z \rightarrow \lambda_{\text{cr}}/2$ ,  $\rho(r, z)$  approaches  $\rho_{\text{1D}}(r)$ , the density profile of a 1D, isothermal filament (Stodolkiewicz 1963; Ostriker 1964). Thus, the quantity given by equation (10) approaches  $N_p = \lambda_{\text{cr}} \rho_{\text{1D}}(0)$  in that limit, declining to zero for smaller  $Z$ . At larger  $Z$ , the isodensity contours are prolate (inside the tidal lobe; outside, they have an open topology), and approach a spherical shape at the largest  $Z$ . The latter equilibria are the most centrally-concentrated of the sequence.

Regarding the corresponding behavior of the mass, we first calculated the isodensity surface corresponding to the half-maximum of the column density; i.e., the contour corresponding to  $N_p/2$ . Let the polar and equatorial radii of the enclosed volume be denoted by  $z_{1/2}$  and  $r_{1/2}$ , respectively. The bounding surface is the analogue to the FWHM intensity contour of the observations. The enclosed mass,  $M_{1/2}$ , can then be found by direct integration.

Figure 6 shows the behavior of  $N_p$  and  $M_{1/2}$  as a function of  $q (= r_{1/2}/z_{1/2})$  in a log-log plot. The polar column density is remarkably flat over the range of  $q$  examined, while  $M_{1/2}$  is an increasing function of  $q$ , as expected.<sup>8</sup> The dotted line shows the  $I_p \propto q^{-0.6}$  best-fit dependence derived from the Monte Carlo simulations. It is reassuring that there is qualitative agreement of  $N_p$  with this line for  $q \gtrsim 0.25$ . The behavior of  $M_{1/2}$  is also qualitatively consistent with expectation, as it has a positive slope ( $\simeq 1.25$ ) toward  $q = 1$ . However, the latter slope disagrees quantitatively with the prediction of equation (9) above, which gives a maximum slope of  $(m+1)(1+C) = 0.40(1.17) = 0.47$  for the M01 sample.

Hence it appears that the results of the shape analysis can be reconciled, at least qualitatively, with one theoretical model of prolate cores. As the latter is undoubtedly among the most

simple one can construct, it remains to be seen whether more realistic models can provide an equal or even superior level of agreement.

### 6.2. Non-Random Orientation

Here we examine the consequences of relaxing the other principal assumption of this work: that of random orientation. Dense cores are nearly always found embedded within larger molecular clouds which, in turn, often display a filamentary appearance. For example, in a recent study of Ophiuchus, the major axes of cores detected in  $\text{C}^{18}\text{O}$  were found to correlate with the symmetry axes of the larger filaments, detected in  $^{13}\text{CO}$  (Tachihara et al. 2000). Thus, it may be that all cores within a given filament have roughly the same orientation,  $\theta_0$ , by dint of their embedding. Then, from equations (5) and (6),  $p$  is given by

$$p(q) = [1 - (1 - q^2) \cos^2 \theta_0]^{1/2} \quad (\text{oblate}), \quad (11)$$

$$= q [1 - (1 - q^2) \sin^2 \theta_0]^{-1/2} \quad (\text{prolate}). \quad (12)$$

Now imagine that there exists a distribution of intrinsic axis ratios  $\psi(q)$  that is non-zero at each  $q$ . In the oblate case, this implies a *minimum, non-zero value of  $p$  in the observed distribution of axis ratios*, and so a reduced range of possible  $p$  (e.g., a lack of edge-on objects unless  $\theta_0$  were exactly equal to zero). Indeed, since the median value of  $\theta_0 = \pi/3$  corresponds to a minimum  $p = 0.87$ , it is unlikely that even an intrinsically very flattened object would appear elongated. Conversely, a distribution of oblate cores with only a very few intrinsically round objects is able to reproduce the observed  $\phi(p)$  near  $p = 1$ . While the observed distribution of  $p$  does display a preponderance of values near  $p = 1$ , there is no clear cutoff at lower  $p$  (Figure 1).

On the other hand, equation (12) shows that a distribution of prolate objects still produces the entire possible range of  $p$ . Only for  $\theta_0$  very near  $\pi/2$  does  $p(q)$  rise to near unity at small values of  $q$ . Interestingly, this means that unless the intrinsic distribution  $\psi(q)$  contains a significant number of (intrinsically) nearly round objects, the observed  $\phi(p)$  will be deficient in (apparently) round objects unless  $\theta_0 \simeq \pi/2$ . Moreover, extremely elongated prolate objects should be quite faint (i.e., difficult to distinguish from the background continuum, due to their comparatively low column density), so any observational sample will have a cutoff at some minimum value  $q_{\text{min}}$ , with corresponding apparent ellipticity  $p_{\text{min}} \geq q_{\text{min}}$ . For any  $\theta_0 > 0$  then, the range of  $p$  will be further reduced. The presence of relatively few objects with small  $p$ , and therefore small  $I$ , could lead to an artificial weighting of higher- $I$  objects and therefore a shallower slope than +1 in  $\log I$  vs.  $\log p$ , as is observed. A more detailed examination of inclination effects, with a corresponding analysis of the observed position angle distribution of cores, would be a highly worthwhile undertaking.

### 6.3. Implications for Core Formation in Filaments

As to the implications of these results for star formation generally, a new picture is emerging of pre-stellar condensation occurring predominantly in filaments. Thus, at least initially, the condensations inherit the shape of their surrounding filament, while gaining more mass along the filament axis. As the core grows in mass, its self-gravity pulls it into a more spherical shape, at the same time causing it to detach from the parent

<sup>8</sup>Note that, due to the different choice of bounding surface, the behavior of  $M_{1/2}$  is qualitatively different from that of  $M_{\text{tl}}$ , which has a peak at intermediate  $q$  (Curry 2000).

cloud. Only after this point might the previous paradigm of isolated, low-mass star formation become relevant (Shu, Adams, & Lizano 1987).

Aspects of this picture have been touched upon by previous authors. Schneider & Elmegreen (1979), motivated by the appearance of “globular filaments” in optical extinction maps, proposed that gravitational instability in the filaments produces the denser, embedded globules. In some cases, the latter were approximately equally spaced along the background filament axis (see also Dutrey et al. 1991). Fleck (1992) emphasized that gravity acting on a nonisotropic mass distribution could be responsible for some aspects of the observed shape distribution. However, he claimed that this implied “molecular clouds are not generally in global (three-dimensional) equilibrium.” Further, he argued that, independent of the exact nature of core elongation (e.g., oblate vs. prolate spheroidal), smaller mass objects should be more nearly spherical “and, because of their low self-gravity, shaped by forces other than gravity.” These comments echo those of earlier authors (Lin, Mestel, & Shu 1965; Larson 1985; Bastien et al. 1991), who remarked that prolate configurations might result from the dynamical contraction of initially cylindrical clouds.

However, it is clear that these dynamical scenarios bear little resemblance to the embedded states considered above. First, as a function of increasing core condensation and mass, the intrinsic ellipticity behaves in an opposite manner in the two cases. Second, the embedded states originate from the spontaneous fragmentation of an initial filament which is near marginal stability, *but not dynamically unstable* (Curry 2000). Third, and most obviously, observations do not furnish any examples of filaments with true cylindrical symmetry. Rather, filamentary structure is invariably a characteristic of cloud envelopes, with the core regions displaying significant fragmentation. Finally, we draw attention to a specific mechanism for embedded core formation presented by Balsara et al. (2001). In this scheme, matter is channelled onto a growing core by a magnetic field more or less coincident with the filament axis. Although the accretion occurs on a dynamical timescale in this scenario, it nevertheless gives some indication that these simple theoretical ideas can be extended into more complex physical regimes.

## 7. CONCLUSIONS

Previous studies of dense core morphology, nearly all of which used molecular line data, gave varied results as to the intrinsic shapes of the cores. We have employed recent dust continuum datasets and additional methods of analysis in an effort to clarify the situation. The main conclusions of this work

are as follows:

- (1) The observed distribution of core ellipticities in the combined continuum sample is well fit by a gaussian distribution of intrinsically prolate objects with mean ellipticity  $\langle q \rangle \approx 0.5 \pm 0.2$ .
- (2) In the M01 sample, the peak intensity  $I$  is positively correlated with the apparent ellipticity  $p$ , with a slope in  $\log I$  vs.  $\log p$  of  $0.50 \pm 0.18$ . This slope is shallower than the +1 value expected for an ensemble of randomly-oriented prolate spheroids, each having constant polar intensity  $I_p$ .
- (3) In the same sample, an equally significant correlation (slope =  $0.65 \pm 0.21$ ) is observed between the log of the total flux density  $S$  and  $\log p$ . This shows that both  $I_p$  and the mass of a given core depend on its intrinsic ellipticity,  $q$ .
- (4) Under the assumption that  $I_p = q^m I_0$ ,  $I_0 = \text{constant}$ , Monte Carlo simulations were used to find the value of  $m$ —and the spheroidal shape—that best fits the observed correlation in ( $\log I$ ,  $\log p$ ). The observed slope and rank C.C. are best fit by a prolate ensemble with  $m = -0.60$  and an intrinsic scatter in  $\log I_0 = 0.15$ . No satisfactory fits for oblate spheroids were found.
- (5) The relation  $I_p = q^{-0.6} S_0$  was shown to agree (for  $q \gtrsim 0.25$ ) with the expected polar column density in the embedded prolate equilibrium sequence of Curry (2000).

The chief limitation of the present work is the relatively small number of objects in the M01 sample, and the consequent weakening of the statistical results so obtained. Also, the fact that all of the cores come from mainly filamentary structures found in three regions may be considered a bias. However, if these cores are truly pre-stellar (as suggested by their number distribution as a function of mass; see §1), then this mode of condensation may in fact be reasonably representative of low- and intermediate-mass star formation. The possibility that at least some of these highly embedded objects are aligned with the major axes of their parent filaments is real, and may alter the results presented here in certain respects (§6.2). The addition of new dust continuum data will allow more definitive conclusions to be drawn on each of these key points, and will no doubt aid in the formulation of more sophisticated theoretical models of embedded cloud equilibria.

I am grateful to F. Motte for providing her previously unpublished peak fluxes, and thank Carol Jones for preliminary discussions about this work. Chris McKee, Steve Stahler, and an anonymous referee offered valuable comments that helped improve the original manuscript.

## REFERENCES

- Balsara, D., Ward-Thompson, D., & Crutcher, R.M. 2001, MNRAS, 327, 715  
 Bastien, P., Arcoragi, J.-P., Benz, W., Bonnell, I., & Martel, H. 1991, ApJ, 378, 255  
 Binney, J., & de Vaucouleurs, G. 1981, MNRAS, 194, 679  
 Chini, R., Reipurth, B., Ward-Thompson, D., Bally, J., Nyman, L.-A., Sievers, A., & Billawala, Y. 1997, ApJ, 474, L135  
 Curry, C.L. 2000, ApJ, 541, 831  
 Curry, C.L., & Stahler, S.W. 2001, ApJ, 555, 160  
 David, M., & Verschueren, W. 1987, A&A, 186, 295  
 Dutrey, A., Langer, W.D., Bally, J., Duvert, G., Castets, A., & Wilson, R.W. 1991, A&A, 247, L9  
 Fall, S.M., & Frenk, C.S. 1983, AJ, 88, 1626  
 Fiege, J., & Pudritz, R.E. 2000a, MNRAS, 311, 105  
 Fiege, J., & Pudritz, R.E. 2000b, ApJ, 534, 291  
 Hanawa, T., et al 1993, ApJ, 404, L83  
 Jijina, J., Myers, P.C., & Adams, F.C. 1999, ApJS, 125, 161  
 Johnstone, D., Wilson, C.D., Moriarty-Schieven, G., Joncas, G., Smith, G., Gregersen, E., Fich, M. 2000, ApJ, 545, 327  
 Johnstone, D., Fich, M., Mitchell, G.F., Moriarty-Schieven, G. 2001, ApJ, 559, 307  
 Jones, C., & Basu, S. 2002, ApJ, 569, 280  
 Jones, C., Basu, S., & Dubinski, J. 2001, ApJ, 551, 387  
 Kiguchi, M., Narita, S., Miyama, S.M., & Hayashi, C. 1987, ApJ, 317, 830  
 Larson, R.B. 1985, MNRAS, 214, 379  
 Launhardt, R., & Henning, T. 1997, A&A, 326, 329  
 Lin, C.C., Mestel, L., & Shu, F.H. 1965, ApJ, 142, 1431  
 Lucy, L.B. 1974, AJ, 79, 745  
 Marchant, A.B., & Olson, D.W. 1979, ApJ, 230, L157  
 Merrifield, M., & Binney, J. 1998, Galactic Astronomy (Princeton: Princeton Univ. Press)  
 Merritt, D. 1982, AJ, 87, 1279  
 Motte, F., André, P., & Neri, R. 1998, A&A, 336, 150

- Motte, F., André, P., Ward-Thompson, D., & Bontemps, S. 2001, *A&A*, 372, L41
- Myers, P.C., Fuller, G.A., Goodman, A.A., & Benson, P.J. 1991, *ApJ*, 376, 561
- Nakamura, F., Hanawa, T., & Nakano, T. 1995, *ApJ*, 444, 770
- Noerdlinger, P.D. 1979, *ApJ*, 234, 802
- Olson, D.W., & de Vaucouleurs, G. 1981, *ApJ*, 249, 68
- Ostriker, J. 1964, *ApJ*, 140, 1056
- Press, W.H., Teukolsky, S.A., Vetterling, W.T., & Flannery, B.P. 1992, *Numerical Recipes in Fortran 77: The Art of Scientific Computing* (Cambridge: Cambridge University Press).
- Richstone, D.O. 1979, *ApJ*, 234, 825
- Ryden, B.S. 1996, *ApJ*, 471, 822
- Schneider, S., & Elmegreen, B.G. 1979, *ApJS*, 41, 87
- Shu, F.H., Adams, F.C., & Lizano, S. 1987, *ARA&A*, 25, 23
- Stahler, S.W. 1983, *ApJ*, 268, 165
- Stodolkiewicz, J.S. 1963, *Acta Astron.*, 13, 30
- Tachihara, K., Mizuno, A., & Fukui, Y. 2000, *ApJ*, 528, 817
- Testi, L., & Sargent, A. 1998, *ApJ*, 508, L91
- Tomisaka, K., Ikeuchi, S., & Nakamura, T. 1988b, *ApJ*, 335, 239

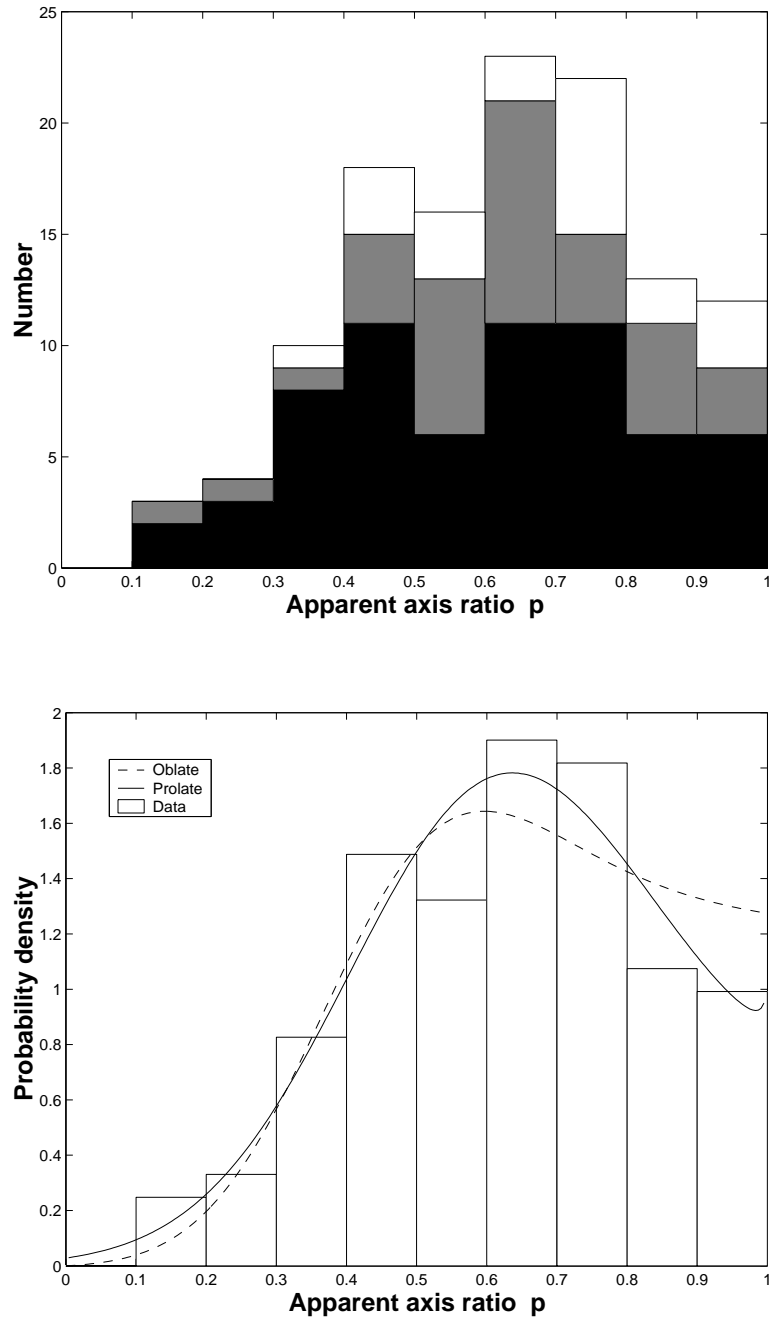


FIG. 1.— (a) The number distribution of apparent axis ratio in the combined continuum sample. The portions belonging to individual samples are indicated in each bin: Motte et al. (2001) (*black*); Motte et al. (1998) (*gray*); Chini et al. (1997) (*white*). The histogram contains 121 cores in total. (b) The best-fit oblate (dashed) and prolate (solid) gaussian distributions to the observed histogram, normalized as a probability density. See text for the best-fit parameters.

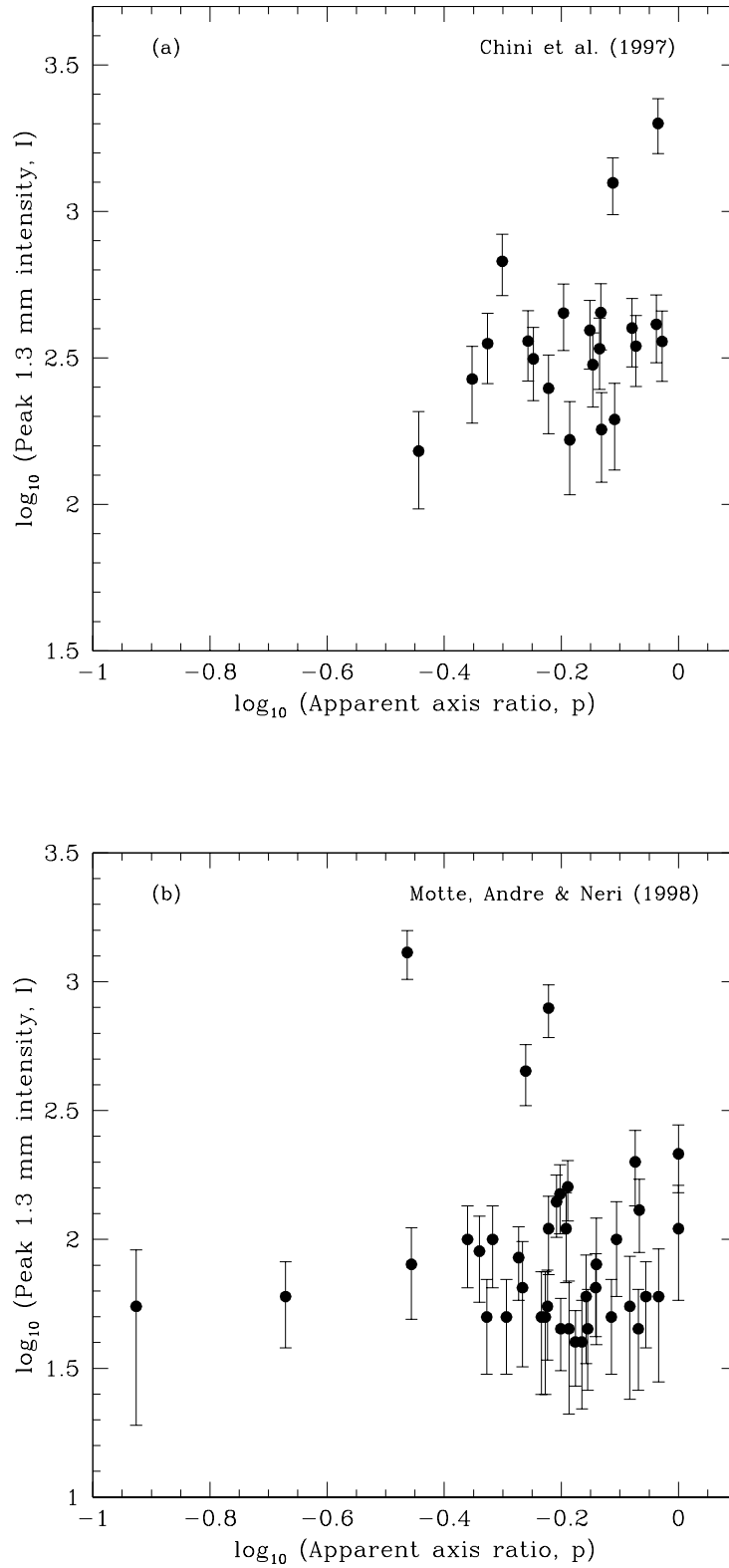


FIG. 2.— (a) Peak intensity as a function of apparent ellipticity for the sample of Chini et al. (1997). (b) Same as (a), but for the sample of Motte et al. (1998). In both samples, the error bars reflect the calibration uncertainty of 20% plus the rms noise cited in the respective papers. Approximate errors in  $\log p$  (omitted for clarity) are  $\pm 0.07$  in (a) and  $\pm 0.05$  in (b).

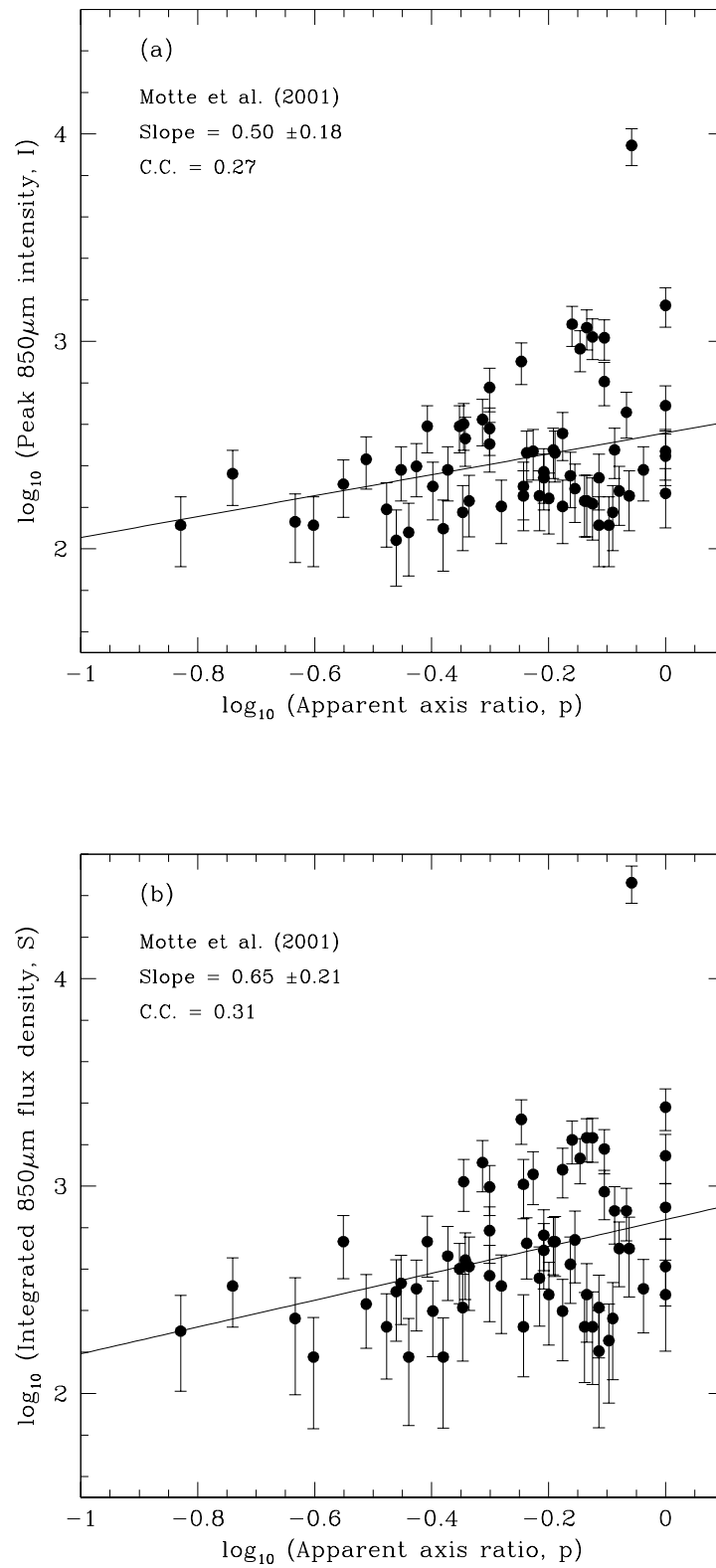


FIG. 3.— (a) Peak intensity as a function of apparent ellipticity for the sample of Motte et al. (2001). (b) Total flux density as a function of apparent ellipticity for the same sample. Error bars in both plots reflect the calibration uncertainty of 20% plus the rms noise cited in §2. Errors in  $\log p$  (omitted for clarity) are  $\pm 0.05$  in both plots.

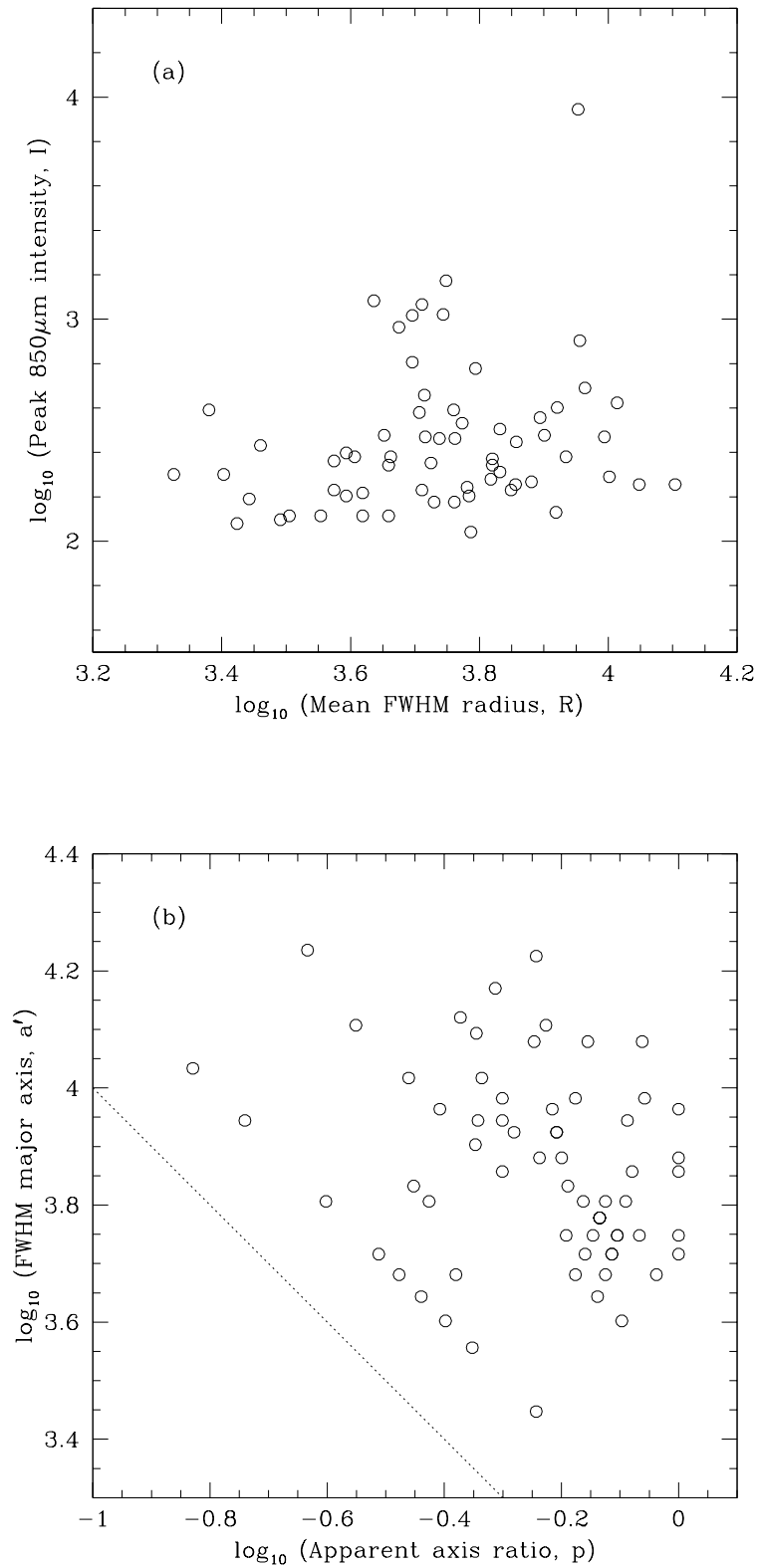


FIG. 4.— (a) Peak intensity as a function of FWHM radius for the sample of M01. (b) FWHM major axis as a function of apparent ellipticity for the same sample. The dotted line has a slope of  $-1$ .

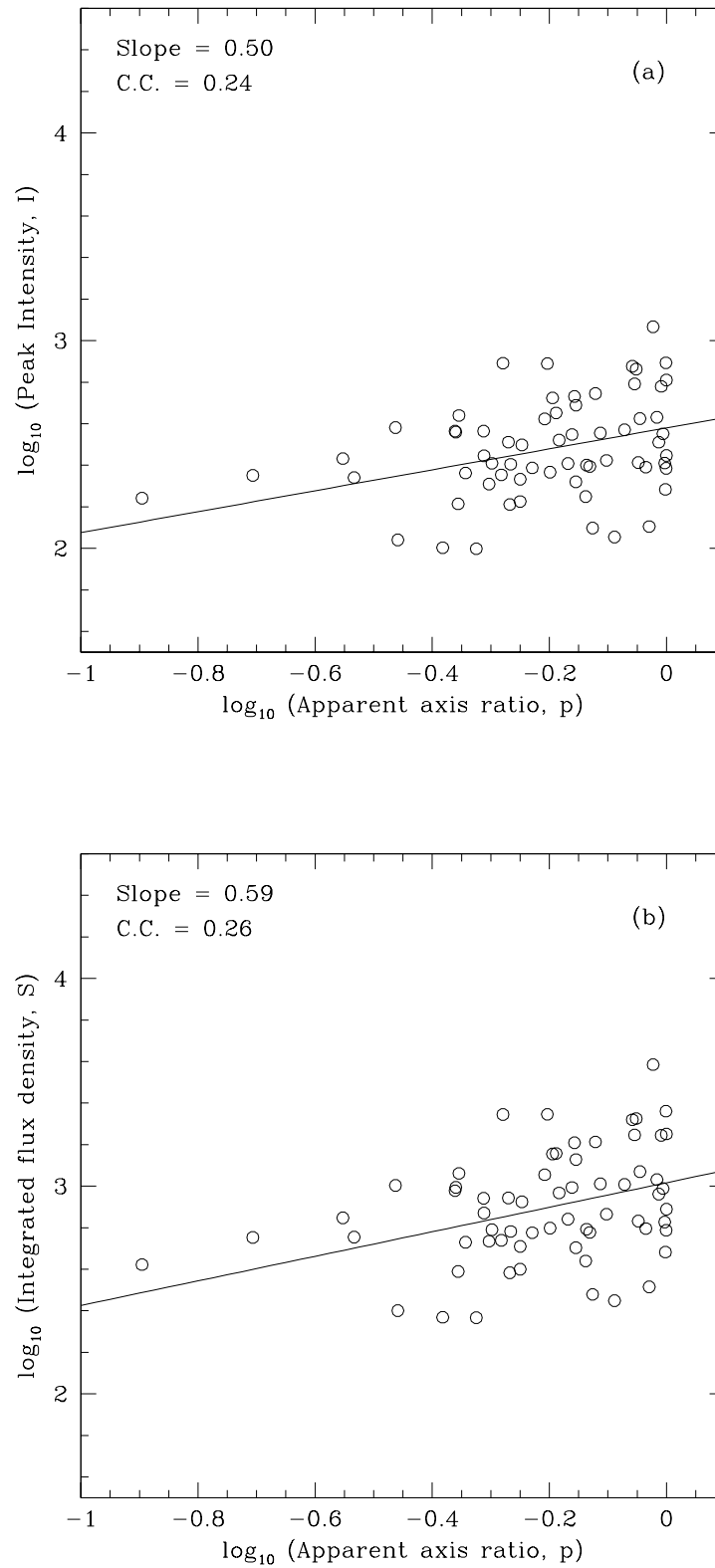


FIG. 5.— (a) One realization from the suite of simulations of  $I$  vs.  $p$  described in §5.5. The correlation coefficient and slope of the least-squares best fit straight line are indicated at upper left. (b) The corresponding  $S$  vs.  $p$  plot for the same simulated dataset.

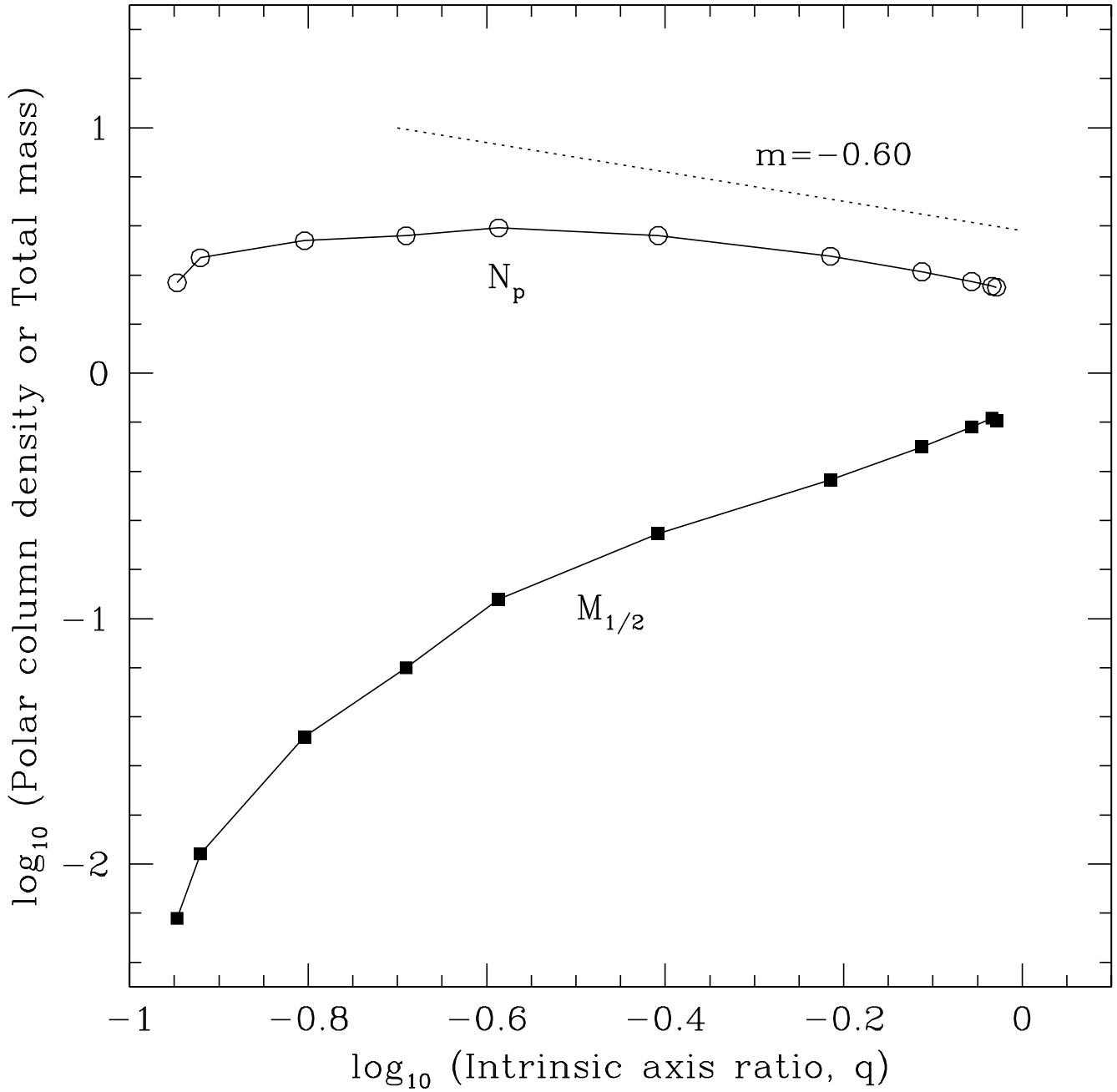


FIG. 6.— Plot of the polar column density  $N_p$  (open circles) and mass  $M_{1/2}$  (filled squares) of cores versus intrinsic axis ratio in the model of Curry (2000). See the text of §6.1 for definitions of these quantities. The dotted line corresponds to the best-fit prolate simulations of  $\log l$  vs.  $\log p$ , and has a slope of  $-0.60$ .

TABLE 1  
SIMULATED LOG  $I$  VERSUS LOG  $p$

| $m$                       | Oblate           |                  | Prolate         |                 |
|---------------------------|------------------|------------------|-----------------|-----------------|
|                           | Slope            | Rank C.C.        | Slope           | Rank C.C.       |
| $\sigma(\log I_0) = 0$    |                  |                  |                 |                 |
| -2                        | $-1.68 \pm 0.44$ | $-0.30 \pm 0.08$ | ...             | ...             |
| -1.5                      | $-1.50 \pm 0.34$ | $-0.33 \pm 0.08$ | ...             | ...             |
| -1                        | $-1.32 \pm 0.25$ | $-0.37 \pm 0.08$ | $0.21 \pm 0.15$ | $0.16 \pm 0.08$ |
| -0.5                      | $-1.15 \pm 0.16$ | $-0.42 \pm 0.08$ | $0.59 \pm 0.12$ | $0.36 \pm 0.07$ |
| 0                         | $-0.97 \pm 0.12$ | $-0.46 \pm 0.07$ | $0.97 \pm 0.11$ | $0.48 \pm 0.07$ |
| 0.5                       | $-0.79 \pm 0.15$ | $-0.39 \pm 0.07$ | $1.34 \pm 0.13$ | $0.53 \pm 0.06$ |
| 1                         | $-0.62 \pm 0.23$ | $-0.28 \pm 0.08$ | $1.72 \pm 0.17$ | $0.54 \pm 0.07$ |
| 1.5                       | ...              | ...              | $2.10 \pm 0.22$ | $0.54 \pm 0.07$ |
| 2                         | ...              | ...              | $2.48 \pm 0.27$ | $0.53 \pm 0.07$ |
| $\sigma(\log I_0) = 0.15$ |                  |                  |                 |                 |
| -2                        | $-1.66 \pm 0.46$ | $-0.28 \pm 0.08$ | ...             | ...             |
| -1.5                      | $-1.48 \pm 0.36$ | $-0.31 \pm 0.08$ | ...             | ...             |
| -1                        | $-1.31 \pm 0.27$ | $-0.34 \pm 0.08$ | $0.20 \pm 0.17$ | $0.12 \pm 0.08$ |
| -0.5                      | $-1.14 \pm 0.19$ | $-0.37 \pm 0.07$ | $0.58 \pm 0.14$ | $0.29 \pm 0.08$ |
| 0                         | $-0.97 \pm 0.16$ | $-0.39 \pm 0.07$ | $0.96 \pm 0.13$ | $0.41 \pm 0.07$ |
| 0.5                       | $-0.79 \pm 0.18$ | $-0.33 \pm 0.07$ | $1.34 \pm 0.15$ | $0.47 \pm 0.07$ |
| 1                         | $-0.62 \pm 0.25$ | $-0.25 \pm 0.08$ | $1.73 \pm 0.18$ | $0.50 \pm 0.07$ |
| 1.5                       | ...              | ...              | $2.11 \pm 0.22$ | $0.51 \pm 0.07$ |
| 2                         | ...              | ...              | $2.49 \pm 0.26$ | $0.51 \pm 0.07$ |

TABLE 2  
SIMULATED LOG  $S$  VERSUS LOG  $p$

| $m$                       | Oblate           |                  | Prolate         |                 |
|---------------------------|------------------|------------------|-----------------|-----------------|
|                           | Slope            | Rank C.C.        | Slope           | Rank C.C.       |
| $\sigma(\log I_0) = 0$    |                  |                  |                 |                 |
| -2                        | $-1.96 \pm 0.51$ | $-0.30 \pm 0.08$ | ...             | ...             |
| -1.5                      | $-1.75 \pm 0.39$ | $-0.34 \pm 0.08$ | ...             | ...             |
| -1                        | $-1.55 \pm 0.28$ | $-0.39 \pm 0.08$ | $0.25 \pm 0.16$ | $0.17 \pm 0.08$ |
| -0.5                      | $-1.34 \pm 0.18$ | $-0.45 \pm 0.07$ | $0.69 \pm 0.12$ | $0.40 \pm 0.07$ |
| 0                         | $-1.13 \pm 0.12$ | $-0.50 \pm 0.07$ | $1.13 \pm 0.11$ | $0.52 \pm 0.06$ |
| 0.5                       | $-0.93 \pm 0.17$ | $-0.42 \pm 0.07$ | $1.57 \pm 0.14$ | $0.56 \pm 0.06$ |
| 1                         | $-0.72 \pm 0.26$ | $-0.30 \pm 0.08$ | $2.01 \pm 0.19$ | $0.56 \pm 0.06$ |
| 1.5                       | ...              | ...              | $2.46 \pm 0.25$ | $0.55 \pm 0.07$ |
| 2                         | ...              | ...              | $2.90 \pm 0.31$ | $0.54 \pm 0.07$ |
| $\sigma(\log I_0) = 0.15$ |                  |                  |                 |                 |
| -2                        | $-1.94 \pm 0.53$ | $-0.29 \pm 0.08$ | ...             | ...             |
| -1.5                      | $-1.74 \pm 0.42$ | $-0.31 \pm 0.08$ | ...             | ...             |
| -1                        | $-1.53 \pm 0.31$ | $-0.35 \pm 0.07$ | $0.23 \pm 0.19$ | $0.13 \pm 0.08$ |
| -0.5                      | $-1.33 \pm 0.21$ | $-0.39 \pm 0.07$ | $0.68 \pm 0.15$ | $0.31 \pm 0.07$ |
| 0                         | $-1.13 \pm 0.17$ | $-0.41 \pm 0.07$ | $1.12 \pm 0.14$ | $0.43 \pm 0.07$ |
| 0.5                       | $-0.93 \pm 0.20$ | $-0.35 \pm 0.07$ | $1.57 \pm 0.16$ | $0.49 \pm 0.07$ |
| 1                         | $-0.72 \pm 0.28$ | $-0.26 \pm 0.07$ | $2.02 \pm 0.20$ | $0.52 \pm 0.07$ |
| 1.5                       | ...              | ...              | $2.47 \pm 0.25$ | $0.52 \pm 0.07$ |
| 2                         | ...              | ...              | $2.91 \pm 0.30$ | $0.52 \pm 0.07$ |